THE ASTROPHYSICAL JOURNAL, 564:176–189, 2002 January 1

A *CHANDRA* X-RAY STUDY OF CYGNUS A. II. THE NUCLEUS

ANDREW J. YOUNG, ANDREW S. WILSON,[1] AND YUICHI TERASHIMA[2]
Astronomy Department, University of Maryland, College Park, MD 20742
KEITH A. ARNAUD[3]
NASA Goddard Space Flight Center, Laboratory for High Energy Astrophysics, Code 660, Greenbelt, MD 20771
AND
DAVID A. SMITH
Astronomy Department, University of Maryland, College Park, MD 20742
Received 2001 June 25; accepted 2001 September 5

ABSTRACT

We report *Chandra* Advanced CCD Imaging Spectrometer and quasi-simultaneous *Rossi X-Ray Timing Explorer* (*RXTE*) observations of the nearby, powerful radio galaxy Cygnus A, with the present paper focusing on the properties of the active nucleus. In the *Chandra* observation, the hard (>a few keV) X-ray emission is spatially unresolved with a size $\lesssim 1''$ (1.5 kpc, $H_0 = 50$ km s^{-1} Mpc^{-1}) and coincides with the radio and near-infrared nuclei. In contrast, the soft (<2 keV) emission exhibits a bipolar nebulosity that aligns with the optical bipolar continuum and emission-line structures and approximately with the radio jet. In particular, the soft X-ray emission corresponds very well with the [O III] λ5007 and Hα + [N II] $\lambda\lambda$6548, 6583 nebulosity imaged with *Hubble Space Telescope*. At the location of the nucleus, there is only weak soft X-ray emission, an effect that may be intrinsic or result from a dust lane that crosses the nucleus perpendicular to the source axis. The spectra of the various X-ray components have been obtained by simultaneous fits to the six detectors. The compact nucleus is detected to 100 keV and is well described by a heavily absorbed power-law spectrum with $\Gamma_h = 1.52^{+0.12}_{-0.12}$ (similar to other narrow-line radio galaxies) and equivalent hydrogen column $N_{\rm H}({\rm nuc}) = 2.0^{+0.1}_{-0.2} \times 10^{23}$ cm^{-2}. This column is compatible with the dust obscuration to the near-infrared source for a normal gas-to-dust ratio. The soft (<2 keV) emission from the nucleus may be described by a power-law spectrum with the same index (i.e., $\Gamma_l = \Gamma_h$), although direct fits suggest a slightly larger value for Γ_l. Narrow emission lines from highly ionized neon and silicon, as well as a "neutral" Fe Kα line, are detected in the nucleus and its vicinity ($r \lesssim 2$ kpc). The equivalent width (EW) of the Fe Kα line (182^{+40}_{-54} eV) is in good agreement with theoretical predictions for the EW versus $N_{\rm H}$(nuc) relationship in various geometries. An Fe K edge is also seen. The *RXTE* observations indicate a temperature of $kT = 6.9^{+0.3}_{-1.0}$ keV for the cluster gas (discussed in Paper III of this series) and cluster emission lines of Fe Kα and Fe Kβ and/or Ni Kα.

We consider the possibility that the extended soft X-ray emission is electron-scattered nuclear radiation. Given that 1% of the unabsorbed 2–10 keV nuclear radiation would have to be scattered, the necessary gas column [$N_{\rm H}$(scattering) $\simeq 3.5 \times 10^{22}$ cm^{-2}] would absorb the X-rays rather than scatter them if the gas is cold. Thus, the scattering plasma must be highly ionized. If this ionization is achieved through photoionization by the nucleus, the ionization parameter $\xi > 1$ ergs cm s^{-1} and the electron density $n_e \simeq 6$ cm^{-3} given the observed distance of the soft X-ray emission from the nucleus. The electron column density inferred from the X-ray observations is much too low to account for the extended optical scattered light, strongly suggesting that the polarized optical light is scattered by dust. The presence of highly ionized Ne lines in the soft X-ray spectrum requires 20 ergs cm s$^{-1} \lesssim \xi \lesssim 300$ ergs cm s^{-1}; these lines may originate closer to the nucleus than the extended soft continuum or in a lower density gas. A collisionally ionized thermal model of the extended soft X-rays cannot be ruled out but is unattractive in view of the low metal abundance required ($Z = 0.03\ Z_\odot$).

The hard X-ray to far-infrared ratio for the nucleus of Cygnus A is similar to that seen in Seyfert 1 and unobscured radio galaxies. By means of the correlation between hard X-ray luminosity and nuclear optical absolute magnitude for these classes of object, we estimate $M_B = -22.4$ for Cygnus A, near the borderline between Seyfert galaxies and QSOs.

Subject headings: galaxies: active — galaxies: individual (Cygnus A) — galaxies: nuclei — X-rays: galaxies

1. INTRODUCTION

Cygnus A (3C 405) is the closest and best studied of the powerful "classical double" (FR II) radio galaxies. At a heliocentric redshift of $z = 0.0562$ (Stockton, Ridgway, &

[1] Adjunct Astronomer, Space Telescope Science Institute, 3700 San Martin Drive, Baltimore, MD 21218.
[2] Institute of Space and Astronautical Science, 3-1-1 Yoshinodai, Sagamihara, Kanagawa 229-8510, Japan.
[3] Also at Astronomy Department, University of Maryland, College Park, MD 20742.

Lilly 1994), it is the most powerful radio source in the 3C catalog out to $z \simeq 1$ and about 1.5 orders of magnitude more luminous than any other 3C source within $z \leq 0.1$. It is interesting for a number of reasons, including (1) radio "hot spots," the shocked jet material at the termini of the jets, were first observed in Cygnus A (Hargrave & Ryle 1974); (2) the galaxy may be at the center of a cooling flow in a cluster of galaxies (Arnaud et al. 1984; Reynolds & Fabian 1996); and (3) there is evidence for a "buried quasar" in the nucleus (Djorgovski et al. 1991; Ward et al. 1991; Antonucci, Hurt, & Kinney 1994; Ueno et al. 1994; Ogle et al. 1997). In this paper we present new *Chandra* X-ray observations of the nucleus and circumnuclear environment of Cygnus A.

In the past there has been debate concerning the nature of the nucleus and circumnuclear regions (approximately the central 4″ [6 kpc]) of Cygnus A, in particular, the central bipolar optical morphology. Suggested explanations have included (1) the merger of two galaxies (Baade & Minkowski 1954), (2) the intersection of a single galaxy by a dust lane (Osterbrock 1983), or (3) a bipolar scattering nebula (see, e.g., Stockton et al. 1994). The presently favored model is that at least some of the central optical morphology results from scattering of light from a hidden nucleus located at the radio core. In the following paragraphs we summarize the key observations of the nucleus and nuclear environment at radio, X-ray, infrared, optical, and ultraviolet wavelengths.

Radio observations with the Very Large Array (VLA) at 6 cm wavelength with 0.″4 resolution (Perley, Dreher, & Cowan 1984) show a compact radio core with a knotty, one-sided jet running along position angle (P.A.) 284° ± 2° from ∼1″–25″. Higher resolution VLBI observations show a "core" with a parsec-scale jet that is aligned with the kiloparsec-scale jet to within 4° (Carilli, Bartel, & Linfield 1991).

Near-infrared imaging shows an unresolved nucleus, within 1″ of the radio core and suggested to be obscured by $A_V \simeq 50 \pm 30$ mag of extinction (Djorgovski et al. 1991). Near-infrared spectroscopy by Ward et al. (1991) detected emission in narrow molecular hydrogen lines, Paα and Brγ. Using an empirical relationship between broad Hα flux and X-ray luminosity for quasars with little reddening and an observed upper limit to the flux of broad Paα, these authors estimate an extinction $A_V(\mathrm{BLR}) > 24$ mag to the broad-line region. A similar relationship between X-ray luminosity and near-infrared luminosity, along with an assumption about the spectral slope of the nuclear spectrum, implies an extinction of $A_V(\mathrm{nuc}) \simeq 54 \pm 9$ mag to the nuclear continuum source (Ward et al. 1991). A more recent study suggests $A_V \sim 150$–200 mag to the nucleus (Ward 1996). For a standard dust-to-gas ratio, $A_V(\mathrm{mag}) = 5 \times 10^{-22} N_{\mathrm{H}}$ (cm^{-2}); this value of A_V implies an obscuring column density of $N_{\mathrm{H}} \simeq 3 \times 10^{23}$ cm^{-2} to the nucleus.

Within the central few arcseconds of Cygnus A, there is an optical source with a bipolar morphology, the northwest component being dominated by line emission and the southeast component being dominated by continuum emission (see, e.g., Stockton et al. 1994). In a *Hubble Space Telescope* (*HST*) *V*-band image (Jackson et al. 1996), the central component resembles the apex of a conical structure similar to that seen in other galaxies and attributed to light from a hidden nucleus escaping along a restricted range of solid angle, i.e., an "ionization cone."

Ultraviolet observations with the *HST* Faint Object Spectrograph by Antonucci et al. (1994) show noisy, broad [Mg II] with an FWHM ∼ 7500 km s^{-1}, which is suggestive of a hidden broad-line region. Subsequent optical spectroscopic observations using Keck II (Ogle et al. 1997) show polarized continuum and broad Balmer-line emission, with the continuum polarization in the northwest component rising to ∼16% at 3800 Å. The polarized light comes from a biconical structure with an opening half-angle in the range 46°–55°, corresponding to the "ionization cone" seen with *HST*. The symmetry of the polarization vectors indicates that this light originated in the nucleus and has been scattered into our line of sight.

Cygnus A is surrounded by cluster gas, and this makes a determination of the X-ray spectrum of the nucleus difficult. The findings of previous X-ray studies of the nucleus and cluster gas of Cygnus A are summarized in Table 1. The detection of a hard power law is compelling evidence for a hidden active nucleus or quasar in the nucleus of Cygnus A, and the values found for the intrinsic column density are typical of Seyfert 2 galaxies (Awaki et al. 1991; Smith & Done 1996; Turner et al. 1997a). Also, Arnaud (1996) showed that the hard X-rays come from a point source within 30″ of the radio core.

In this paper, we focus on *Chandra* X-ray observations of the nucleus of Cygnus A. Our results on the X-ray emission from the radio hot spots and the intracluster gas are discussed by Wilson, Young, & Shopbell (2000, hereafter Paper I) and Smith et al. (2002, hereafter Paper III), respectively, while a future paper will deal with the cavity inflated by the radio jets. A Hubble constant of $H_0 = 50$ km s^{-1} Mpc^{-1} and a deceleration parameter of $q_0 = 0$ have been

TABLE 1

PREVIOUS X-RAY SPECTRAL MODELS OF THE NUCLEUS AND CLUSTER GAS OF CYGNUS A

Observatory	Reference	N_{H} (nuc) (cm^{-2})	Γ (nuc)	L_{X}(nuc)[a] (ergs s^{-1})	kT(cluster) (keV)	L_{X}(cluster)[a] (ergs s^{-1})
EXOSAT/HEAO 1.....	1	$8.2^{+10.0}_{-3.0} \times 10^{22}$	1.7[b] (1.78[c])	5.3×10^{44}	$4.1^{+5.6}_{-1.5}$	6.7×10^{44}
Ginga	2	$3.75^{+0.75}_{-0.71} \times 10^{23}$	$1.98^{+0.18}_{-0.20}$	1.1×10^{45}	$7.3^{+1.8}_{-1.3}$	1.2×10^{45}
ROSAT HRI.....	3	8.2×10^{22}[b]		3.6×10^{45}		
ASCA	4	$1.1^{+2.1}_{-0.6} \times 10^{23}$	$1.80^{+0.28}_{-0.43}$	2.5×10^{44}	$7.6^{+1.5}_{-1.5}$	9.9×10^{44}
		$1.5^{+2.1}_{-0.9} \times 10^{23}$	$1.76^{+0.35}_{-0.34}$	7.9×10^{44}	$8.4^{+1.3}_{-1.4}$	8.9×10^{44}

[a] Over energy range 2–10 keV.
[b] Parameter fixed.
[c] Value if allowed to vary.
REFERENCES.—(1) Arnaud et al. 1987. (2) Ueno et al. 1994. (3) Harris, Perley, & Carilli1994. (4) Sambruna et al. 1999.

assumed throughout. The luminosity and "angular size" distances to Cygnus A are then 346.4 and 310.6 Mpc, respectively, and 1″ corresponds to 1.51 kpc.

2. OBSERVATIONS AND REDUCTION

2.1. *Observations*

The nucleus of Cygnus A is known to be a strong X-ray source, and we were concerned that "pile-up" would affect the *Chandra* observations. In order to obtain the count rate of the nucleus and circumnuclear regions, we first obtained a short observation (Obs. ID 359) of Cygnus A on 2000 March 8 using chip S3 (backside illuminated) of the Advanced CCD Imaging Spectrometer (ACIS; Garmire et al. 2000). Single exposures with a 0.1 s frame time were alternated with two exposures with a 0.4 s frame time, the total integration time being $\lesssim 1$ ks. This observation showed the nucleus was not significantly piled-up in either the 0.1 or 0.4 s frame time, but the observed count rate indicated that a 3.2 s frame-time observation of the nucleus would suffer from significant pile-up. On this basis, we decided to observe Cygnus A for separate, longer exposures with frame times of 0.4 and 3.2 s, which were designed to study primarily the X-ray emission of the nucleus and the larger scale regions, respectively. The resulting level 1 and level 2 peak count rates in the long exposure 3.2 s frame-time observation (see below) are 0.0425 and 0.0286 counts pixel^{-1} s^{-1}, respectively. Thus, only 67% of the events were good grades, a clear indication of pile-up. In contrast, the level 2 and level 1 peak count rates in the long 0.4 s frame-time exposure are 0.053 and 0.056 counts pixel^{-1} s^{-1}, respectively, indicating about 94% good grades. The higher count rate in the 0.4 s than the 3.2 s frame time is also an indicator of pile-up in the 3.2 s frame-time observation.

These longer integrations were taken with the ACIS instrument in two separate observations. On 2000 May 21 (Obs. ID 360), the standard 3.2 s frame time was used. CCDs I2, I3, S1, S2, S3, and S4 were read out, although most of the X-ray emission from Cygnus A is on S3. On 2000 May 26 (Obs. ID 1707), a subarray window 128 pixels wide on the S3 chip was used with a 0.4 s frame time to mitigate the effects of pile-up in the inner regions, as discussed above. Both exposures were taken with Cygnus A at the aim point of the S3 chip. The data were screened in the usual way for times of high background count rates and aspect errors. The 3.2 and 0.4 s frame-time data have total good exposure times of 34,720 and 9227 s, respectively. Spectra and instrument responses were generated using CIAO 2.1 (with reprocessed data) and CALDB 2.3, and analyzed with XSPEC, Version 11.0.1. The *Chandra* response is not reliable below 0.45 keV, although the backside-illuminated S3 chip has good sensitivity to X-rays down to 0.1 keV. To improve the sampling of the X-ray images, we interpolated the data from the original 0.″5 to 0.″05 sized pixels and then smoothed the resulting image with a Gaussian of FWHM 0.″5.

Cygnus A was also observed using the *Rossi X-Ray Timing Explorer* (*RXTE*) on 2000 May 20. Data were gathered using the Proportional Counter Array (PCA) and High-Energy X-Ray Timing Experiment (HEXTE). Two PCA counters (PCU0 and PCU2) were operating at the time of the observation, but PCU0 had suffered the loss of its propane layer 1 week earlier. Because a good background subtraction model is not yet available for PCU0 in this new state, we have restricted our analysis to PCU2. We used the standard Rex script[4] to generate PCA and HEXTE light curves, source and background spectra, and response matrices. Both the PCA and HEXTE have a field of view of 1° (FWHM) and are sensitive to photons in the ranges 2–60 and 15–250 keV, respectively. The PCA and HEXTE have a spectral resolution of $\Delta E/E \simeq 18\%$ at 6 and 60 keV, respectively. The good exposure times were 29.3 ks for the PCA and 9.7 ks for each of the two HEXTE clusters.

2.2. *Extraction Regions*

To obtain a *Chandra* spectrum of the nucleus, counts were extracted from a 2.″5 diameter circle centered on the peak of the X-ray emission. In the 0.4 s frame-time data, there are 2781 counts, corresponding to a count rate of 0.301 ± 0.006 counts s^{-1}. Background counts were extracted from a concentric annulus with an inner diameter 7″ and outer diameter 20″. The background level is very low and is equivalent to only 43 counts, 1.5% of the total within the 2.″5 diameter circle used for the nucleus.

In order to investigate the spectrum of the circumnuclear extended regions, we took counts from two sectors of a circle with diameter 7″ centered on the nucleus. The sectors have half-angles of 55°, and their axes are aligned with the jet and counter jet. In the 0.4 s frame-time data, there are 3183 counts, corresponding to a count rate of 0.345 ± 0.006 counts s^{-1}, within these sectors. Background counts were extracted from a concentric annulus with inner diameter 7″ and outer diameter 14″. The background level is equivalent to 224 counts, 8% of the total inside the two sectors. The source extraction regions contain some flux from the nucleus.

3. X-RAY MORPHOLOGY

The X-ray morphology within the central 4″ × 4″ around the nucleus varies strongly with photon energy (see Fig. 1). Above approximately 2 keV, the nucleus appears to be pointlike and coincident with the radio core (see § 5), while below ~ 1 keV a bipolar distribution is clearly seen in the higher signal-to-noise ratio 3.2 s frame-time data, with one peak of emission $\simeq 1.''2$ northwest of the nucleus along P.A. 287^{+35}_{-13} deg and a second peak $\simeq 1.''3$ southeast of the nucleus along P.A. 115^{+30}_{-21} deg. These are the position angles of the center of the brightest pixels, in the 0.25–1 keV image, to the northwest and southeast relative to the location of the nucleus and determined using the IRAF CENTER tool. The quoted "error bars" are the range of position angle given by moving $\sqrt{2}$ pixels from the peak pixel diagonally northeast and southwest. The bipolar distribution is easily seen in a color image (Fig. 2), in which the data are divided into three bands, red representing 0.1–1.275 keV, green 1.275–2.2 keV, and blue 2.2–10 keV. Images in the three bands were then combined to give the overall color picture. The nuclear region has a blue, and hence hard, X-ray pointlike core, with the two offset regions to the northwest and southeast appearing yellower, indicative of softer X-ray emission. Even though a clear bipolar morphology is seen, there is also soft X-ray emission close to the nucleus. A comparatively smooth distribution of hot gas is projected around the nuclear region.

The double morphology may be due, in part, to the presence of a dust lane running north-south across the nucleus

[4] See http://RXTE.gsfc.nasa.gov/docs/xte/recipes/rex.html.

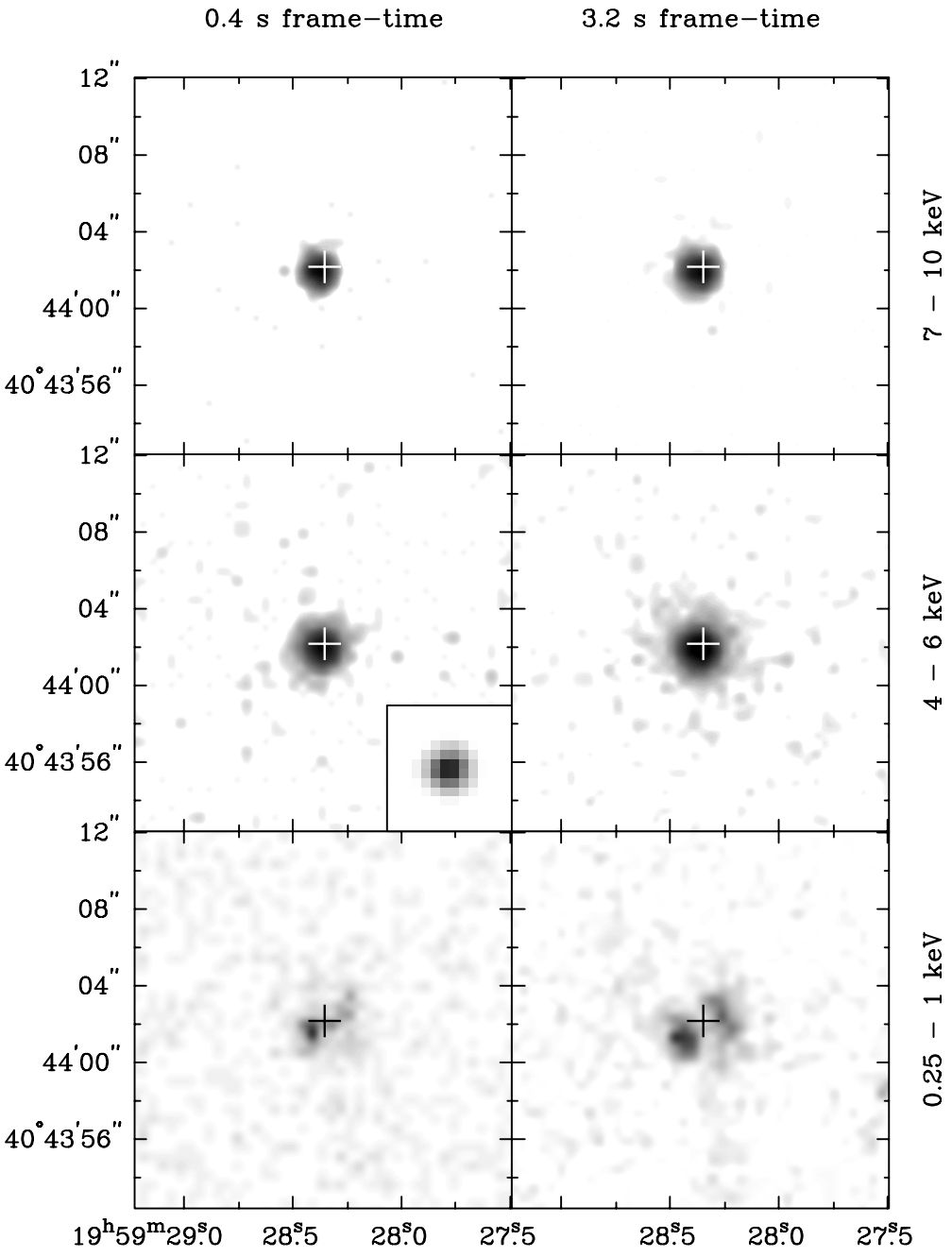

FIG. 1.—Gray-scale representations of *Chandra* X-ray images of the nucleus of Cygnus A in three energy bands and for each of the two frame times used. The *Chandra* images have been resampled to 10 times smaller pixel size and smoothed by a Gaussian of FWHM 0.″5. The left column has a 0.4 s frame time and the right column a 3.2 s frame time. In the top row the energy range is 7–10 keV, the center row 4–6 keV, and the bottom row 0.25–1 keV. The center left panel also shows the PSF at 4.51 keV. The plus symbol indicates the location of the peak of the hard X-ray emission that has been aligned with the radio core. The look-up tables for the gray scale are different in each panel, with the upper two rows having a logarithmic scale and the bottom row a linear scale.

obscuring the central $\sim 1''$ of the soft X-ray emission. The 0.25–1 keV flux per pixel at the location of the nucleus is approximately 40% of that at the peak of the soft X-ray emission some $\sim 1.''2$ from the nucleus. If the intrinsic luminosity and spectra of these two regions are the same, then a modest additional column density of $N_{\rm H}$(cold gas in dust lane) $\simeq 2.4 \times 10^{21}$ cm^{-2} obscuring the nucleus would be sufficient to account for the lower flux at the nucleus. This column density is consistent with the additional reddening of the nucleus by the dust lane (Shaw & Tadhunter 1994; Tadhunter, Metz, & Robinson 1994), assuming a standard dust-to-gas ratio.

To determine whether *Chandra* resolves the pointlike, hard X-ray nucleus, its radial profile was compared with a model of the point-spread function (PSF). It should be noted that on larger spatial scales, significant X-ray emission is observed in the neighborhood of the nucleus. Most of this larger scale emission is thermal in origin with a temperature of 4–5 keV and apparently represents emission from the intracluster gas projected close to the nucleus (Paper III). This hot plasma has a significant high-energy tail, so the wings of the PSF from the nucleus may merge into the continuum emission from the thermal plasma. To minimize this effect, the PSF was calculated at 8.6 keV,

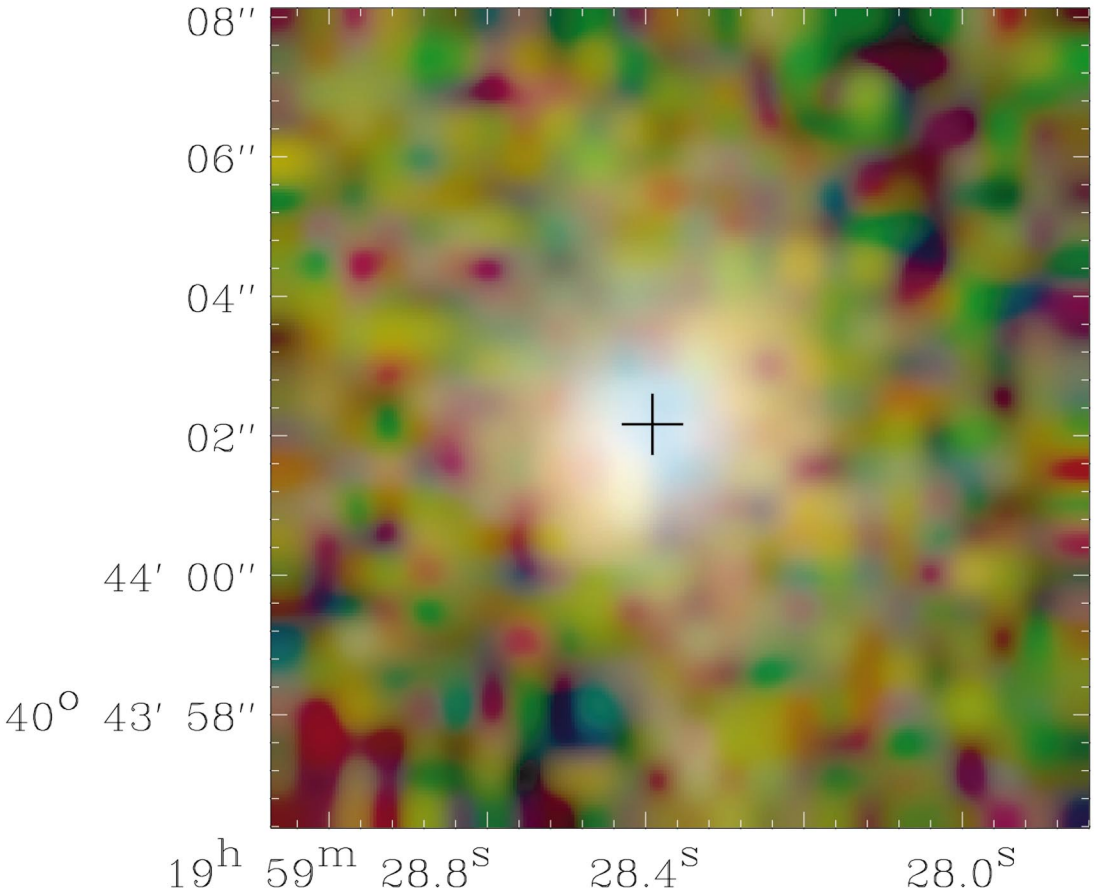

FIG. 2.—Color representation of the *Chandra* X-ray image of the nucleus of Cygnus A. The image has been resampled to 10 times smaller pixel size and smoothed by a Gaussian of FWHM 0.″5. The data were divided into three bands, red representing 0.1–1.275 keV, green 1.275–2.2 keV, and blue 2.2–10 keV. The nuclear region has a blue (hard) pointlike core with two offset regions of softer emission. This emission is embedded in a comparatively smooth distribution of hot gas. The plus symbol indicates the location of the peak of the hard X-ray emission that has been aligned with the radio core.

where the contribution from the cluster gas is much smaller than at lower energies. The background level was determined using a circle of radius 22.″5 offset 50″ southeast of the nucleus. Radial profiles of the PSF at 8.6 keV and the observed 7–9 keV counts (from the 0.4 s frame-time data) centered on the nucleus are shown in Figure 3. The hard X-ray nucleus is seen to be unresolved.

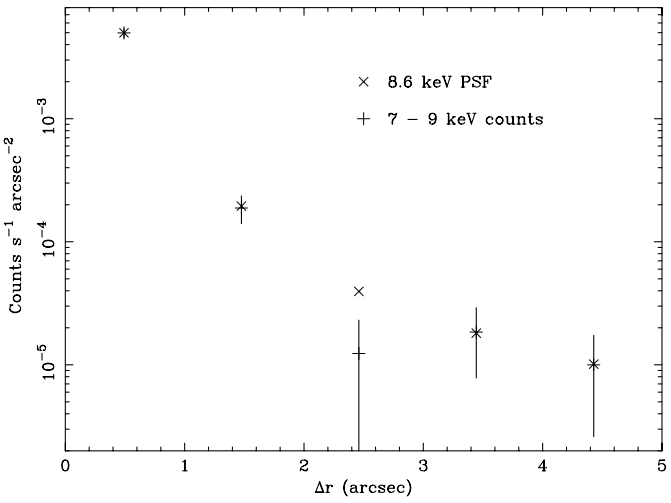

FIG. 3.—Radial profile of counts from the nucleus of Cygnus A extracted from the 0.4 s frame-time data in the energy range 7–9 keV (*plus symbol points with Poissonian error bars*) compared to the theoretically computed PSF at 8.6 keV (*multiplication symbol points*). The data indicate that the hard X-ray source in the nucleus is unresolved.

4. X-RAY SPECTRA

4.1. *Nucleus*

The grossly different spatial resolutions of *Chandra* and *RXTE* mean that different spectral models have to be fitted to data sets from each observatory. The 2.″5 diameter circle used to extract counts from the *Chandra* data effectively isolates the nucleus from the surrounding cluster, whereas the $\simeq 1^\circ$ resolution of *RXTE* yields a spectrum that includes the nucleus, features associated with the radio source, and the intracluster gas. The *Chandra* data show the "hot spots" to have $\lesssim 1\%$ of the 7–10 keV flux of the nucleus, so flux from the "hot spots" will not contribute significantly to the *RXTE* spectrum. The *Chandra* and *RXTE* spectra are shown in Figure 4. The *Chandra* spectrum of the nucleus has two main components—a soft component below 2 keV and a hard component above 2 keV. In the previous section, we noted that the soft component is spatially extended and the hard component spatially unresolved. Additionally, there is a strong iron line around 6.4 keV in the rest frame of Cygnus A. The *Chandra* spectrum was modeled over the energy range 0.7–9 keV. The *RXTE* spectra cover a much larger spatial area and extend up to much higher energies. The PCA spectra were fitted over

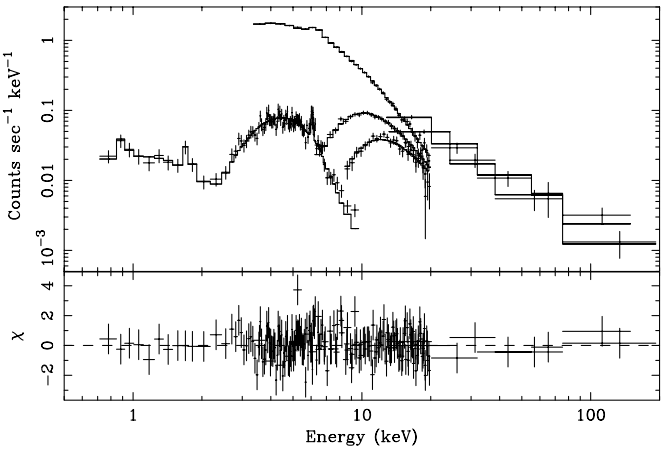

FIG. 4.—X-ray spectra of Cygnus A extracted from the 0.4 s frame-time *Chandra* data and the *RXTE* data. The energy scale is as observed. The upper panel shows the data points with error bars (*crosses*), with the model folded through the instrument responses (*solid lines passing through the data points*). The lower panel shows the χ residuals from this fit. The parameters of the model ("Model 1") are listed in Table 2. The spectrum over the range 0.7–9 keV is the *Chandra* observation of the nucleus through a circular aperture of diameter 2".5 with a 0.4 s frame time. The curve near the top of the figure at 3 keV and extending from 3 to 20 keV is the *RXTE* layer 1 PCA spectrum; that extending from 6 to 20 keV is the layer 2 PCA spectrum; and that extending from 8 to 20 keV is the layer 3 PCA spectrum. The HEXTE spectrum extends from 12 to 200 keV.

energy ranges of 3–20 keV (layer 1), 6–20 keV (layer 2) and 8–20 keV (layer 3). The HEXTE spectra were fitted over the energy range 15–200 keV and grouped (using the FTOOL GRPPHA) into bins such that the signal-to-noise ratio in each bin exceeded 40 [i.e., $(s_i - b_i)/(s_i + b_i)^{1/2} > 40$, where s_i are the measured source counts and b_i are the background counts in bin i]. The various spectral components were modeled as follows: (1) a heavily absorbed power law (with photon index Γ_h, where h stands for "high energy") to represent the hidden quasar; (2) either a power law (with photon index Γ_l, where l stands for "low energy") plus narrow emission lines ("model 1") or a bremsstrahlung plus narrow emission lines ("model 2"), all absorbed by the Galactic column density [assumed here to be $N_{\rm H}({\rm Gal}) = 3.3 \times 10^{21}$ cm^{-2}; Dickey & Lockman 1990], to describe the extended soft X-ray emission (there is only very marginal evidence for intrinsic absorption of this emission—see § 4.2); (3) a "neutral" iron fluorescence line; and (4) a high-temperature bremsstrahlung with two narrow emission lines to represent the thermal emission of the intracluster gas. Components (1), (2), and (3) were fitted to all of the data sets, while component (4) was fitted to only the *RXTE* data sets. The six data sets—one *Chandra*, three *RXTE* PCA, and two *RXTE* HEXTE—were modeled simultaneously using XSPEC, with the relative normalizations of the *Chandra*, PCA, and HEXTE data allowed to vary. The parameters of these models are listed in Table 2. All quantities refer to the rest frame of Cygnus A, with the exception of the column density to the low-energy nuclear emission, which refers to the observer's frame. The relative normalizations in Table 2 give the factors by which the calibrated spectra from the various instruments have been multiplied to provide the best fit. The factor for *Chandra* is defined to be 1.0, and those for the *RXTE* detectors are close to or consistent with unity.

In model 1, the low energy (<2 keV) part of the nuclear spectrum is modeled with a power law, the photon index (Γ_l) of which is constrained to be the same as that (Γ_h) of the high-energy power law describing the hidden nucleus. Such would be the case if the low-energy emission represents

TABLE 2

SPECTRAL MODELS OF THE NUCLEUS AND CLUSTER GAS OF CYGNUS A

Model Component	Parameter	Model 1	Model 2
Column density to low energy emission (nucleus).....	$N_{\rm H}$ (cm^{-2})	$1.9^{+1.7}_{-1.0} \times 10^{21}$	3.3×10^{21} [a]
Low energy (<2 keV) bremsstrahlung (nucleus)	kT (keV)		$6.6^{+\infty}_{-5.2}$
	$K_{\rm Brem}$ [b]		$9.5^{+4.8}_{-1.3} \times 10^{-5}$
Low energy (<2 keV) power-law (nucleus)	Γ_l	$1.52^{+0.12}_{-0.12}$ [c]	
	$K_{\rm PL}$ [d]	$6.0^{+1.7}_{-1.1} \times 10^{-5}$	
Column density to nucleus	$N_{\rm H}$ (cm^{-2})	$2.0^{+0.1}_{-0.2} \times 10^{23}$	$2.0^{+0.1}_{-0.2} \times 10^{23}$
High energy power-law (nucleus)	Γ_h	$1.52^{+0.12}_{-0.12}$	$1.53^{+0.12}_{-0.15}$
	$K_{\rm PL}$ [d]	$5.2^{+1.6}_{-1.1} \times 10^{-3}$	$5.3^{+1.6}_{-1.0} \times 10^{-3}$
Bremsstrahlung (cluster gas)[e]	kT (keV)	$6.9^{+0.3}_{-1.0}$	$6.8^{+0.5}_{-0.8}$
	$K_{\rm Brem}$ [b]	$2.3^{+0.5}_{-0.3} \times 10^{-2}$	$2.3^{+0.4}_{-0.3} \times 10^{-2}$
Relative normalizations	*Chandra*	1.00	1.00
	RXTE PCA	$1.31^{+0.75}_{-0.26}$	$1.34^{+0.39}_{-0.31}$
	RXTE HEXTE	$1.08^{+0.31}_{-0.07}$	$1.10^{+0.51}_{-0.11}$
Fit statistic.....	χ^2/dof	181/185	177/184

[a] Parameter fixed at Galactic column density.

[b] The term $K_{\rm Brem} = 3.02 \times 10^{-15} \int n_e n_I dV/4\pi D_A^2$, where n_e is the electron density (cm^{-3}), n_I is the ion density (cm^{-3}), and D_A is the angular size distance to the source (cm).

[c] Fixed to the same value as found for Γ_h.

[d] The term $K_{\rm PL}$ = photons cm^{-2} s^{-1} keV^{-1} at 1 keV.

[e] The cluster gas contributes significantly to only the *RXTE* data sets.

electron-scattered light from the hidden nucleus. This model provides an excellent description of the data with a χ^2 of 181 for 185 degrees of freedom (dof). In model 2, the low-energy part of the spectrum is modeled as bremsstrahlung emission. This also provides an excellent description of the data with a χ^2 of 177 for 184 dof (Table 2). In both models the hidden nucleus is described by a power law, the best-fit value of which has $\Gamma_{h1}(= \Gamma_{l1}) = 1.52^{+0.12}_{-0.12}$ (the subscript 1 denotes "model 1"), $\Gamma_{h2} = 1.53^{+0.12}_{-0.15}$ (the subscript 2 denotes "model 2"), obscured by a column density of $2.0^{+0.1}_{-0.2} \times 10^{23}$ cm^{-2}. These values of Γ are consistent with that obtained—$\Gamma_l = 1.80^{+1.1}_{-1.1}$—by simply modeling the soft (0.6–2.5 keV) spectrum by an absorbed power law. The HEXTE data alone are well described by a power law of photon index $\Gamma_h = 1.48^{+0.36}_{-0.34}$, between 20 and 200 keV. These values for Γ_h are similar to those found for unobscured active galactic nuclei (AGNs), such as Seyfert 1 galaxies. The unabsorbed rest-frame 2–10 keV luminosity of the hidden nucleus in Cygnus A is L_X(nuc) = 3.7×10^{44} ergs s^{-1} and its 0.5–2 keV luminosity 1.5×10^{44} ergs s^{-1}. In model 1, the soft X-ray component is absorbed by a column density of $1.9^{+1.7}_{-1.0} \times 10^{21}$ cm^{-2}, which is nominally lower than but consistent with the Galactic value. The *Chandra* data show soft X-ray lines from He-like and/or H-like Ne and ionized Si from the nucleus (see Table 3). A strong, narrow nuclear Fe Kα fluorescence line is seen at $6.40^{+0.05}_{-0.03}$ keV, consistent with Fe II–Fe XVIII. If the line width is a free parameter, we obtain $\sigma_{\rm Fe} = 0.09^{+0.03}_{-0.04}$ keV, which is not significantly broad, and comparable to the detector resolution at 6 keV, $\sigma_{\rm detector} \simeq 0.08$ keV.[5] The EW of the Fe line, 182^{+40}_{-54} eV, is in excellent agreement with theoretical predictions for the EW versus $N_{\rm H}$(nuc) relation in various geometries (see Fig. 3 of Ptak et al. 1996). A strong, nuclear, iron absorption edge is observed at a rest-frame energy of approximately 7.2 keV, corresponding to the K-shell edge of Fe I–Fe X (see Fig. 5). If the iron abundance in the absorbing gas is allowed to vary (using the VPHABS model in XSPEC), the best-fitting value is found to be Z(Fe) = $0.90^{+0.46}_{-0.48}$ $Z_\odot$(Fe). In addition, there is tentative evidence for an iron Kβ line at a rest-frame energy of 7.1 keV, and this will add to the uncertainty in the estimate of the iron abundance.

[5] In the present calibration the FWHM of the line response is systematically narrower than the data, so $\sigma_{\rm Fe}$ is consistent with zero.

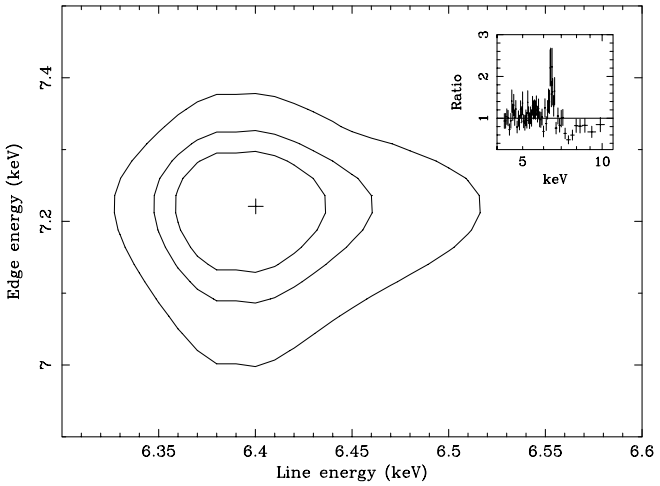

FIG. 5.—Confidence contours (plotted at 68%, 90% and 99%) of the rest-frame energy of the iron line and absorption edge from modeling the 0.4 s frame-time *Chandra* data. The aperture is a circle of diameter 2.″5. The line energy is consistent with that of the Fe Kα fluorescence line of neutral iron. The absorption edge is consistent with that of iron in the range Fe I–Fe X. The panel in the upper right shows the ratio of the *Chandra* data to a power law as a function of rest-frame energy. To produce this panel, the data were modeled by a power law from 4 to 9 keV.

The temperature of the thermal emission from the cluster gas, measured by the *RXTE* instruments, is $kT_1 = 6.9^{+0.3}_{-1.0}$ keV, $kT_2 = 6.8^{+0.5}_{-0.8}$ keV, and the unabsorbed rest-frame 2–10 keV luminosity of the cluster is L_X(cluster) = 1.2×10^{45} ergs s^{-1}. These parameters for the cluster are in good agreement with the results from *Ginga* (Ueno et al. 1994), *EXOSAT* (Arnaud et al. 1987), and *ASCA* (Sambruna, Eracleous, & Mushotzky 1999; Markevitch et al. 1998; Markevitch, Sarazin, & Vikhlinin 1999). The cluster flux that we measure with *RXTE* is larger than that

TABLE 3

EMISSION LINES FROM THE NUCLEUS (*Chandra*, APERTURE DIAMETER 2.″5) AND CLUSTER GAS (*RXTE*, SPATIAL RESOLUTION $\simeq 1°$)

Model	Location	Energy (keV)	Line	Rest-Frame Energy (keV)	K[a]	EW (eV)
1.....	Nucleus	0.90–1.02	Ne IX triplet–Ne X	$0.97^{+0.03}_{-0.06}$	$6.0^{+9.6}_{-4.9} \times 10^{-6}$	90[b]
1.....	Nucleus	1.76–1.86	Si VII–Si XIII	$1.83^{+0.02}_{-0.06}$	$3.7^{+2.3}_{-2.3} \times 10^{-6}$	148[b]
1.....	Nucleus	6.40–6.44	Fe II–Fe XVIII	$6.40^{+0.05}_{-0.03}$	$5.9^{+1.4}_{-1.8} \times 10^{-5}$	182[c]
1.....	Cluster gas	6.65–6.69	Fe XXIV–Fe XXV	$6.70^{+0.04}_{-0.04}$	$2.9^{+0.9}_{-0.6} \times 10^{-4}$	444[d]
1.....	Cluster gas	7.70–8.08	Ni XXV–Ni XXVIII	$7.90^{+0.21}_{-0.22}$	$5.0^{+0.9}_{-1.5} \times 10^{-5}$	115[d]
		7.68–7.88	Fe XXII Kβ–Fe XXV Kβ			
2.....	Nucleus	0.90–0.92	Ne IX triplet	$0.92^{+0.07}_{-0.02}$	$1.7^{+0.6}_{-1.2} \times 10^{-5}$	202[e]
2.....	Nucleus	1.76–1.86	Si VII–Si XIII	$1.83^{+0.03}_{-0.07}$	$3.3^{+2.7}_{-2.4} \times 10^{-6}$	109[e]
2.....	Nucleus	6.40–6.44	Fe II–Fe XVIII	$6.41^{+0.04}_{-0.04}$	$6.6^{+0.9}_{-2.4} \times 10^{-5}$	202[c]
2.....	Cluster gas	6.65–6.69	Fe XXIV–Fe XXV	$6.70^{+0.05}_{-0.05}$	$2.7^{+0.4}_{-0.7} \times 10^{-4}$	434[d]
2.....	Cluster gas	7.70–8.08	Ni XXV–Ni XXVIII	$7.90^{+0.19}_{-0.17}$	$4.8^{+1.3}_{-1.2} \times 10^{-5}$	115[d]
		7.74–7.88	Fe XXIII Kβ–Fe XXV Kβ			

[a] The term K = photons cm^{-2} s^{-1} in the line.
[b] With respect to the unabsorbed low-energy power-law component.
[c] With respect to the unabsorbed high-energy power-law component.
[d] With respect to the unabsorbed bremsstrahlung component modeling the cluster emission.
[e] With respect to the unabsorbed low-energy bremsstrahlung component.

found from modeling the *Chandra*-detected emission in chip S3 (an 8′ × 8′ region of the inner part of the cluster gas—see Paper III) since the field of view of *RXTE* is much larger than that of *Chandra*. The model of the cluster gas includes two strong emission lines, one at a rest-frame energy of 6.70 keV from ionized Fe Kα and another at 7.90 keV (see Table 3) that may be either or both ionized Fe Kβ and ionized Ni Kα.

4.2. *Northwest and Southeast Regions*

In order to study the extended soft X-ray emission within a few arcseconds of the nucleus, we obtained a spectrum from the 0.4 s frame-time data using two sectors of a circle with diameter 7″ centered on the nucleus. The sectors had half-angles of 55°, and their axes were aligned with the jet and counter jet (see Fig. 1, *bottom panels*). We restrict our attention to the energy range 0.5–2 keV to minimize the contribution from the unresolved nucleus. The spectrum was initially modeled by a hot thermal plasma with solar metal abundances using the MEKAL model in XSPEC, absorbed by the Galactic column. This model provides a very poor fit to the data (see Table 4) and may be ruled out. If the metal abundances are allowed to vary, the best model has an abundance of only 3% of solar, which is implausible. Bremsstrahlung or power-law models, both absorbed by the Galactic column, are also unsatisfactory (Table 4).

A power law plus narrow emission lines, all absorbed by the Galactic column, provides a much better description of the data (see Tables 4 and 5 and Fig. 6), with a χ^2 value of 22 for 21 dof. The photon index of the power law, $\Gamma_l = 2.01^{+0.46}_{-0.54}$, is consistent with that obtained through the 2.″5 aperture but marginally steeper than that found for the heavily absorbed nuclear source at high energy, $\Gamma_h = 1.52^{+0.12}_{-0.12}$ (model 1) or $\Gamma_h = 1.53^{+0.12}_{-0.15}$ (model 2; see Table 2). For the power law plus narrow emission lines model, the unabsorbed rest-frame 0.5–2 keV luminosity is 3.8×10^{42} ergs s^{-1} and, by extrapolating to higher energies with $\Gamma_l = 2.01$, the unabsorbed rest-frame 2–10 keV luminosity is found to be 3.7×10^{42} ergs s^{-1} (7″ diameter, double-sector aperture). For comparison, the power law plus lines model through the 2.″5 aperture (model 1) has a rest-frame 0.5–2 keV luminosity, corrected for Galactic absorption, of 2.0×10^{42} ergs s^{-1} and, by extrapolating the low-energy

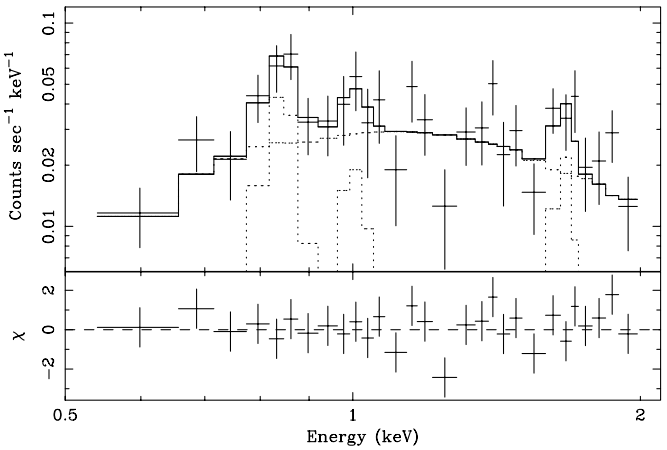

FIG. 6.—X-ray spectrum of the soft extended nuclear emission of Cygnus A extracted from the 0.4 s frame-time data (§ 4.2). The aperture consisted of two sectors of a circle with diameter 7″ centered on the nucleus, each sector having an opening half-angle of 55° and their axes aligned with the jet and counter jet. The energy scale is as observed. The upper panel shows the data points with error bars (*crosses*) and the model folded through the instrument response (*uppermost solid line passing through the data points*). The individual components of the model are plotted below this with dotted lines. The lower panel shows the χ residuals to this fit. The parameters of this model are listed in Tables 4 and 5.

TABLE 4

SPECTRAL MODELS OF THE NORTHWEST AND SOUTHEAST CIRCUMNUCLEAR REGIONS (TWO SECTORS, DIAMETER 7″)

Frame Time (s)	Model	$N_{\rm H}$ (cm^{-2})	kT (keV)	Abundance ($Z_\odot$)	Γ_l	Normalization[a]	χ^2/dof
0.4.....	MEKAL	3.3×10^{21} [b]	$4.9^{+5.9}_{-1.9}$	1.00[c]		$K_{\rm MEKAL} = 3.7^{+0.6}_{-0.6} \times 10^{-4}$	50/27
0.4.....	MEKAL	3.3×10^{21} [b]	$1.5^{+1.5}_{-0.5}$	$0.03^{+0.24}_{-0.03}$		$K_{\rm MEKAL} = 6.4^{+2.6}_{-2.0} \times 10^{-4}$	44/26
0.4.....	Brem	3.3×10^{21} [b]	$1.5^{+1.5}_{-0.5}$			$K_{\rm Brem} = 2.1^{+0.9}_{-0.5} \times 10^{-4}$	44/27
0.4.....	PL	3.3×10^{21} [b]			$2.17^{+0.36}_{-0.38}$	$K_{\rm PL} = 1.4^{+0.1}_{-0.2} \times 10^{-4}$	42/27
0.4.....	PL + lines	3.3×10^{21} [b]			$2.01^{+0.46}_{-0.54}$	$K_{\rm PL} = 1.1^{+0.2}_{-0.2} \times 10^{-4}$	22/21

[a] Model normalizations are $K_{\rm MEKAL} = 10^{-14}/\{4\pi[D_A(1+z)]^2\}\int n_e n_{\rm H}\, dV$, where n_e is the electron density (cm^{-3}), $n_{\rm H}$ is the hydrogen density (cm^{-3}), and D_A is the angular size distance to the source (cm); $K_{\rm Brem} = 3.02 \times 10^{-15}\int n_e n_I\, dV/4\pi D_A^2$, where n_e is the electron density (cm^{-3}), n_I is the ion density (cm^{-3}), and D_A is the angular size distance to the source (cm); and $K_{\rm PL}$ = photons cm^{-2} s^{-1} keV^{-1} at 1 keV.

[b] Fixed at the Galactic column.

[c] Parameter fixed.

TABLE 5

EMISSION LINES FROM THE NORTHWEST AND SOUTHEAST CIRCUMNUCLEAR REGIONS (TWO SECTORS, DIAMETER 7″)

Frame Time (s)	Energy (keV)	Line	Rest-Frame Energy (keV)	K[a]	EW (eV)
0.4.....	0.89–0.92	Ne VII–Ne IX	$0.91^{+0.01}_{-0.02}$	$1.8^{+1.0}_{-0.8} \times 10^{-5}$	127
0.4.....	1.02	Ne X Lyα?	$1.08^{+0.28}_{-0.09}$	$5.5^{+5.1}_{-5.5} \times 10^{-6}$	54
0.4.....	1.74–1.82	Si II–Si XI	$1.76^{+0.06}_{-0.03}$	$4.2^{+3.0}_{-2.7} \times 10^{-6}$	110
0.4.....	6.40–6.44	Fe II–Fe XVIII	$6.39^{+0.03}_{-0.03}$	$5.0^{+0.9}_{-1.8} \times 10^{-5}$	226

[a] The term K = photons cm^{-2} s^{-1} in the line.

power law to higher energies with $\Gamma_l = 1.52$, an unabsorbed rest-frame 2–10 keV luminosity of 4.2×10^{42} ergs s^{-1}.

We observe lines from Ne VII–Ne IX Kα and Si II–Si XI Kα and tentatively detect an H-like Ne Kα line (see Table 5). The spectrum is shown in Figure 6. If we fit a power law from 4–9 keV plus a narrow Gaussian, we find an iron line consistent with Fe II–Fe XVIII Kα with an equivalent width of 226 eV. In the 3.2 s frame-time data we observe two lines, Ne V–Ne IX Kα and Si VII–Si X Kα, consistent with the 0.4 s frame-time data, but do not require the H-like Ne line. The line fluxes from the 3.2 s frame-time observation are too low because of the effects of pile-up, and we do not give them.

It should be noted that the value of Γ_l depends on the assumed absorbing column density. As can be seen from Figure 7, the lower the absorbing column density, the lower the inferred photon index, with an uncertainty of $\Delta N_{\rm H} \simeq 1 \times 10^{21}$ cm^{-2} corresponding to an uncertainty in the photon index of $\Delta\Gamma_l \simeq 0.6$. The precise values of the extinction toward and intrinsic to Cygnus A are difficult to determine, given its low galactic latitude. Within Cygnus A itself the extinction is very patchy (see, e.g., Fig. 7 of Jackson, Tadhunter, & Sparks 1998), while the foreground reddening, measured toward three normal elliptical galaxies in the Cygnus A group, is approximately $E(B-V) = 0.36$ (Spinrad & Stauffer 1982). Assuming a standard gas-to-dust ratio, this foreground extinction corresponds to a column density of 2.2×10^{21} cm^{-2}. If the average absorbing column density over the 7″, double-sector aperture is close to this value instead of the assumed $N_{\rm H}({\rm Gal}) = 3.3 \times 10^{21}$ cm^{-2}, the value of Γ_l becomes $\simeq 1.5$, the same value as found for Γ_h (§ 4.1).

To investigate any spectral differences between the northwest and southeast regions, the circumnuclear emission was divided into two regions. A circle of diameter 10″ centered on the peak of the X-ray emission was divided into two semicircles by a line running along P.A. 14°, which is perpendicular to the radio jet on small scales. Also, a square region of 3 pixels × 3 pixels (1.″5 × 1.″5) centered on the peak pixel was excluded. The 0.4 s frame-time data between 0.5 and 2 keV from each region were modeled by an absorbed power law of fixed photon index $\Gamma = 2.10$ (see Table 4). The best model has column densities of $N_{\rm H}({\rm NW}) = 2.6^{+0.9}_{-0.8} \times 10^{21}$ cm^{-2}, consistent with the Galactic column density toward Cygnus A, and $N_{\rm H}({\rm SE}) = 4.7^{+1.5}_{-1.1} \times 10^{21}$ cm^{-2}. This possible excess column to the southeast side suggests that it is the farther, in agreement with Carilli & Barthel (1996). If real, the difference in absorbing columns would correspond to $\Delta A_V \simeq 1$ mag of optical extinction.

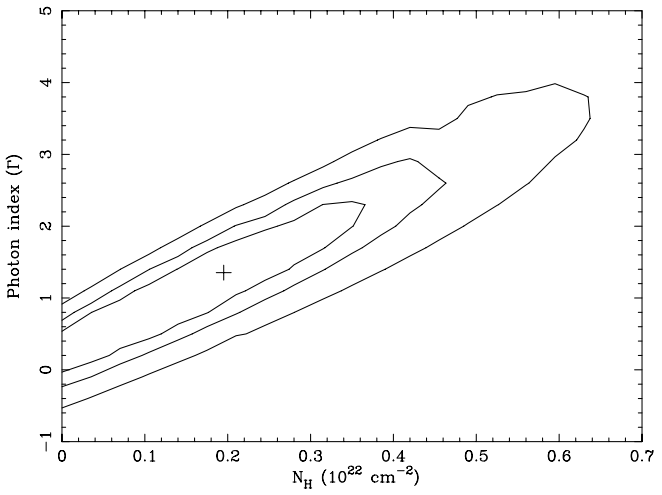

FIG. 7.—Confidence contours of the absorbing column density $N_{\rm H}$ and photon index Γ_l of the soft X-ray emission plotted at 68%, 90%, and 99%. The aperture consists of two sectors of a circle with diameter 7″ centered on the nucleus, each sector having an opening half-angle of 55° and their axes aligned with the jet and counter jet. Note that Γ_l and $N_{\rm H}$ are not independent and an error in the value of the assumed column density will give a corresponding error in the value of Γ_l. The Galactic column density is assumed to be 3.3×10^{21} cm^{-2} in this paper.

5. COMPARISON WITH OBSERVATIONS AT OTHER WAVELENGTHS

The central few arcseconds of Cygnus A contain considerable structure (§ 1). Radio observations (Perley et al. 1984; Carilli et al. 1991) show a compact "core" located at $\alpha_r = 19^{\rm h}59^{\rm m}28^{\rm s}.348$, $\delta_r = 40°44'02''.17$ (J2000.0), with a prominent jet running along P.A. 284° ± 3° (Carilli et al. 1991). We assume the core to be the location of the "true" nucleus, i.e., the putative supermassive black hole and accretion disk. The peak of the X-ray emission, found using the IRAF tool CENTER and the *Chandra* astrometry, is at $\alpha_{\rm X} = 19^{\rm h}59^{\rm m}28^{\rm s}.375$, $\delta_{\rm X} = 40°44'02''.36$ (J2000.0). The offset between these two positions is less than 0.″4 (i.e., smaller than 1 *Chandra* pixel and within the current systematics), and we assume them to be coincident. The *Chandra* images were, therefore, shifted so that the peak of the X-ray emission coincides with the peak of the radio emission. A superposition of the *Chandra* 3.2 s frame-time data on a 6 cm radio map is shown in Figure 8. The two peaks of soft X-ray emission, one $\simeq 1.''2$ along P.A. 287° to the northwest and the other $\simeq 1.''3$ along P.A. 115° to the southeast are, to within a few degrees, along the P.A. of the radio jet and counter jet, respectively. The peak to the northwest coincides with a "neck" in the radio jet and also corresponds to a channel dividing the northwest cloud seen in *HST* images (discussed below). There is evidence of a counter jet in the radio observations (Carilli & Barthel 1996), and this passes just to the north of the southeast X-ray peak.

We recomputed the plate solutions of the infrared K'- and optical r-band images of Stockton et al. (1994) using the known positions of stars in the field of Cygnus A (Griffin 1963). Unsaturated stars c, d, g, and h (using the nomenclature of Griffin 1963) were used for the K′ band and c, d, and g for the r band. Having obtained the plate solution using the stars, the IRAF tool CENTER places the K' nucleus at $\alpha_{K'} = 19^{\rm h}59^{\rm m}28^{\rm s}.378$, $\delta_{K'} = 40°44'02''.09$ (J2000.0), which is within 0.″4 of the radio core and represents coincidence given the errors. The nucleus in the r-band image is not pointlike, so it cannot be simply aligned with the radio core. Instead, the same offset (less than 0.″4) was applied to the r-band image as was applied to the K' image. The r-band image shows bright peaks of emission at the nucleus and to the northwest and southeast. The bright, extended optical emission correlates well with the extended X-ray emission (see Fig. 9).

HST imaging in wavebands containing optical emission lines (Jackson et al. 1994, 1996) reveals three distinct structures in a roughly 4″ × 4″ region around the nucleus. There are two "clouds," one to the northwest and one to the southeast, and a "bar" connecting the southern extreme of the northwest cloud to the northern extreme of the southeast cloud. In the middle of the "bar" there is a bright

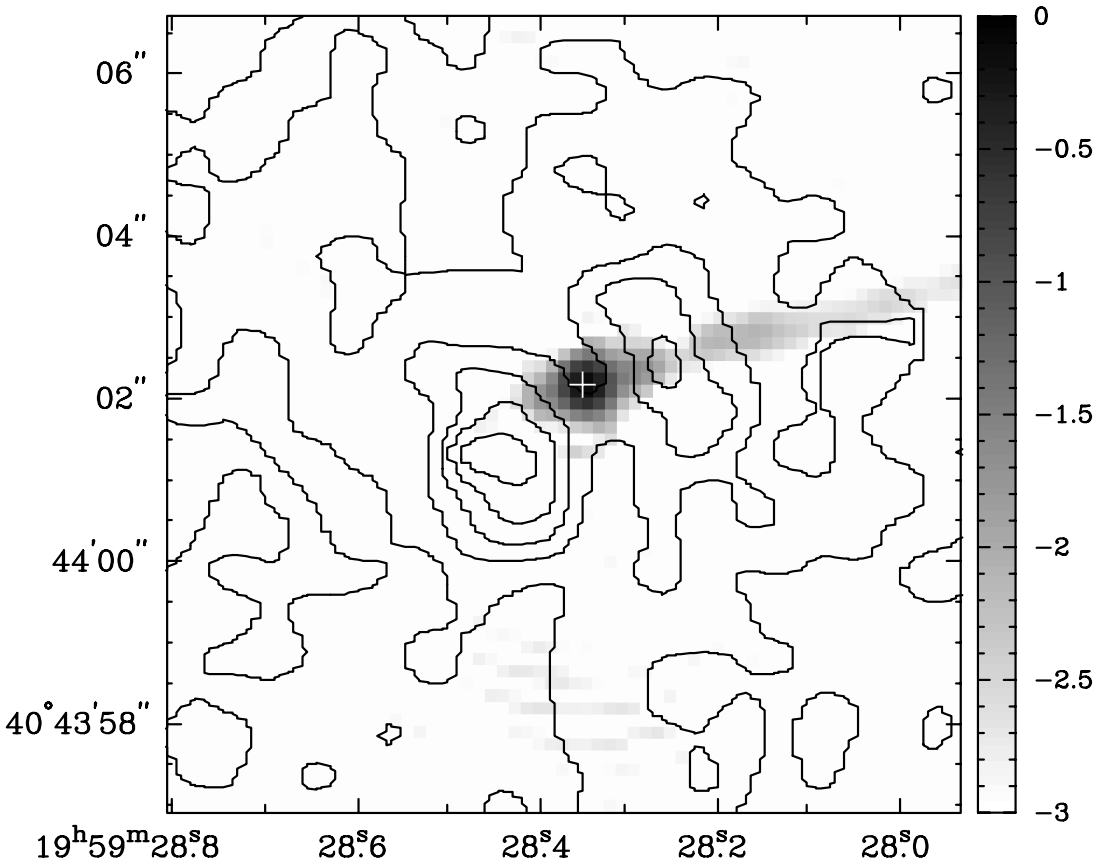

FIG. 8.—Superposition of the *Chandra* 3.2 s frame-time data with events in the range 0.25–1.00 keV (*contours*) on a 6 cm radio map (*gray scale*; Perley et al. 1984). The resolution (FWHM) of the radio map is 0″.4. The contours of the *Chandra* image are plotted at 2, 6, 10, 14, and 18 counts (0″.5 pixel)$^{-1}$. The *Chandra* image has been resampled to 10 times smaller pixel size and then smoothed by a Gaussian of FWHM 0″.5. The gray scale of the radio map is proportional to the logarithm of the intensity between 0.001 (*white*) and 1 Jy beam^{-1} (*black*), as indicated by the vertical bar. Note the neck in the radio jet 1″.2 to the northwest of the nucleus, where it passes through the northwest extended X-ray emission. This neck also corresponds to a channel dividing the northwest cloud seen in *HST* images in bands containing redshifted [O III] λ5007 (see Fig. 10) and Hα (see Fig. 11).

optical knot at $\alpha_{HST} = 19^h59^m28^s.344$, $\delta_{HST} = 40°44'2''.25$ (J2000.0; Jackson et al. 1994), which is within 0″.1 of the radio core. Thus, in aligning the optical, radio, and X-ray images, the central optical component in the *HST* images was assumed to coincide with the radio and X-ray nuclei. There are bright peaks in [O III] λ5007 and Hα + [N II] $\lambda\lambda$6548, 6583 emission coincident with the hard X-ray nucleus and the northern region of the extended X-ray emission to the northwest (see Figs. 10 and 11). Diffuse [O III] line emission is seen from an approximately biconical region centered on the nucleus, and in this regard the X-ray and [O III] emissions appear well correlated (as also found in NGC 1068 [Young, Wilson, & Shopbell 2001], where the ionization of the X-ray–emitting gas is dominated by photoionization [Paerels et al. 2000]).

6. DISCUSSION

6.1. *The Hidden Nucleus*

The *Chandra* observations of the nucleus of Cygnus A identify the source of hard X-ray emission with an unresolved point source located within 0″.4 of and probably coincident with the radio core. The spectrum of this point source is well described by a power law of photon index $\Gamma = 1.5^{+0.12}_{-0.12}$, with rest-frame 2–10 keV luminosity (corrected for absorption) of L_X(nuc) = 3.7×10^{44} ergs s^{-1} obscured by a column density of $2.0^{+0.1}_{-0.2} \times 10^{23}$ cm^{-2}. The power-law slope has been determined with unprecedented precision for Cygnus A and is at the lower end of the distribution of photon indices for narrow-line radio galaxies (see Fig. 2*a* of Sambruna et al. 1999). A narrow Fe Kα line is observed in the energy range of Fe II–Fe XVIII, with an equivalent width of approximately 200 eV. The fact that the hard X-ray power law is detected out to 100 keV confirms the similarity to Seyfert galaxies and quasars. However, we find no evidence for broad Fe Kα.

The above noted value of L_X(nuc) in the 2–10 keV band and the [O III] λ5007 luminosity (2.6×10^{43} ergs s^{-1}, after correction for 1.5 mag of Galactic extinction; see Osterbrock & Miller 1975) are in accordance with the X-ray–[O III] luminosity correlation for Seyfert galaxies and unobscured radio galaxies (e.g., Mulchaey et al. 1994; Sambruna et al. 1999) and are comparable to the two type 2 QSO candidates IRAS 23060+0505 and IRAS 20460+1925 (see Fig. 5 in Halpern, Eracleous, & Forster 1998). The X-ray to far-infrared luminosity ratio in Cygnus A is L_X(2–10 keV)/L_{FIR} = 0.18 and is similar to that of QSOs (e.g., Elvis et al. 1994). The far-infrared luminosity was calculated from the *IRAS* fluxes using $F_{FIR} = 1.26 \times 10^{-14}(2.58S_{60} + S_{100})$ W m^{-2}, where S_{60} and S_{100} are the flux densities at 60 and 100 μm, respectively, in units of janskys.

We attempt to estimate the nuclear optical absolute magnitude, which cannot be measured directly because of the

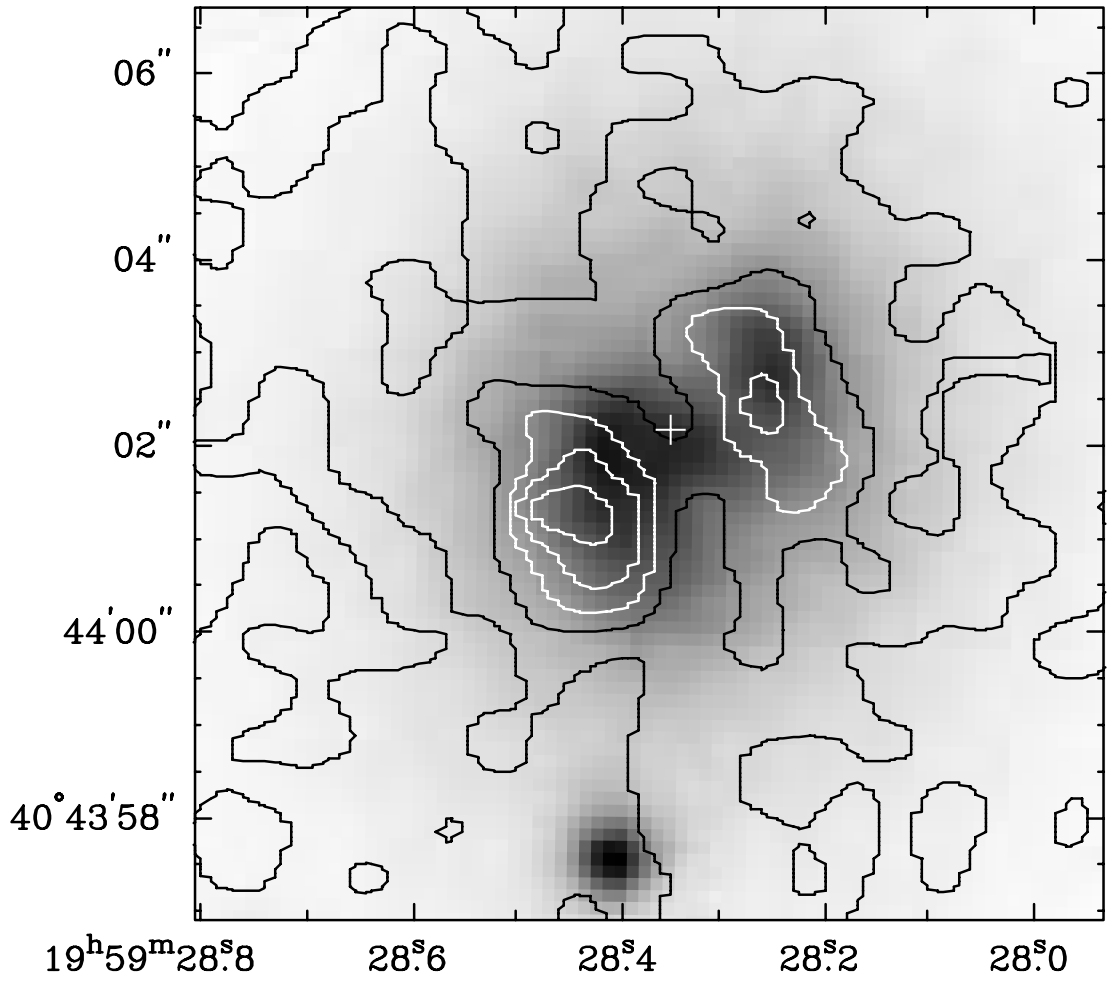

FIG. 9.—Superposition of the *Chandra* 3.2 s frame-time data with events in the range 0.25–1.00 keV (*contours*) on an optical *r*-band image taken through a filter with center wavelength/bandwidth 7531 Å/361 Å (*gray scale*; Stockton et al. 1994). The FWHM seeing for the optical image was 0.″81. The contours of the *Chandra* image are at 2, 6, 10, 14, and 18 counts (0.″5 pixel)$^{-1}$. The *Chandra* image has been resampled to 10 times smaller pixel size and then smoothed by a Gaussian of FWHM 0.″5. The gray scale of the optical image is proportional to the intensity squared between 5×10^{-20} (*white*) and 6×10^{-19} ergs cm^{-2} s^{-1} Å^{-1} (*black*).

heavy extinction toward the nucleus. First, we assume that the spectral energy distribution (SED) of Cygnus A is the same as the median SED of radio-loud quasars presented in Elvis et al. (1994). Then, normalizing to the X-ray flux, the absolute magnitude in the B band is found to be $M_B = -22.4$. Alternatively, the Hβ luminosity–M_B correlation for type 1 Seyfert galaxies and QSOs (Ho & Peng 2001) gives $M_B = -21.2$. Note, however, that the Hβ luminosities adopted in Ho & Peng (2001) are a combination of the broad and narrow components, and the broad component dominates in type 1 QSOs. We used only the narrow component of Hβ for Cygnus A, and therefore this last value of M_B should be regarded as an upper limit (i.e., a lower limit on the B-band luminosity). This upper limit is consistent with the estimate obtained using the SED.

6.2. *Electron-scattered Nuclear Flux*

In this section we discuss the possibility that the extended bipolar soft X-ray continuum emission to the northwest and southeast of the nucleus is electron-scattered nuclear light. In such a model the continuum spectrum of the electron-scattered component is identical to that of the nucleus, and the observations are consistent with the directly viewed hard component and the soft component having the same photon index (i.e., $\Gamma_h = \Gamma_l$, §§ 4.1 and 4.2). An extrapolation of the soft X-ray power law has an unabsorbed rest-frame 2–10 keV luminosity of approximately 3.7×10^{42} ergs s^{-1} (see § 4.2), which corresponds to approximately 1% of the unobscured 2–10 keV nuclear luminosity (3.7×10^{44} ergs s^{-1}; see § 4.1). This is compatible with the range of scattering fractions inferred in Seyfert 2 galaxies, in which typically 0.25%–5% of the nuclear light is hypothesized to be scattered into our line of sight (Turner et al. 1997b), and less than the 5%–10% inferred in those objects exhibiting broad polarized Hα (Awaki et al. 2000); of course, there may be, in addition, intrinsically extended thermal emission. If the X-rays are scattered by an optically thin population of electrons in a biconical region, then

$$L_{\rm scattered} = L_{\rm intrinsic} \frac{\Omega}{4\pi} \tau_{\rm scattering}$$

$$= L_{\rm intrinsic}(1 - \cos\theta)\tau_{\rm scattering},$$

where θ is the opening half-angle of the biconical region, observed by *HST* to be $\theta \simeq 55°$. Using the luminosities given above, we find an optical depth through one cone of $\tau_{\rm scattering} \simeq 0.02$ and a column density $N_e({\rm scattering}) = \tau_{\rm scattering}/\sigma_T = 3.5 \times 10^{22}$ cm^{-2}. This is significantly higher

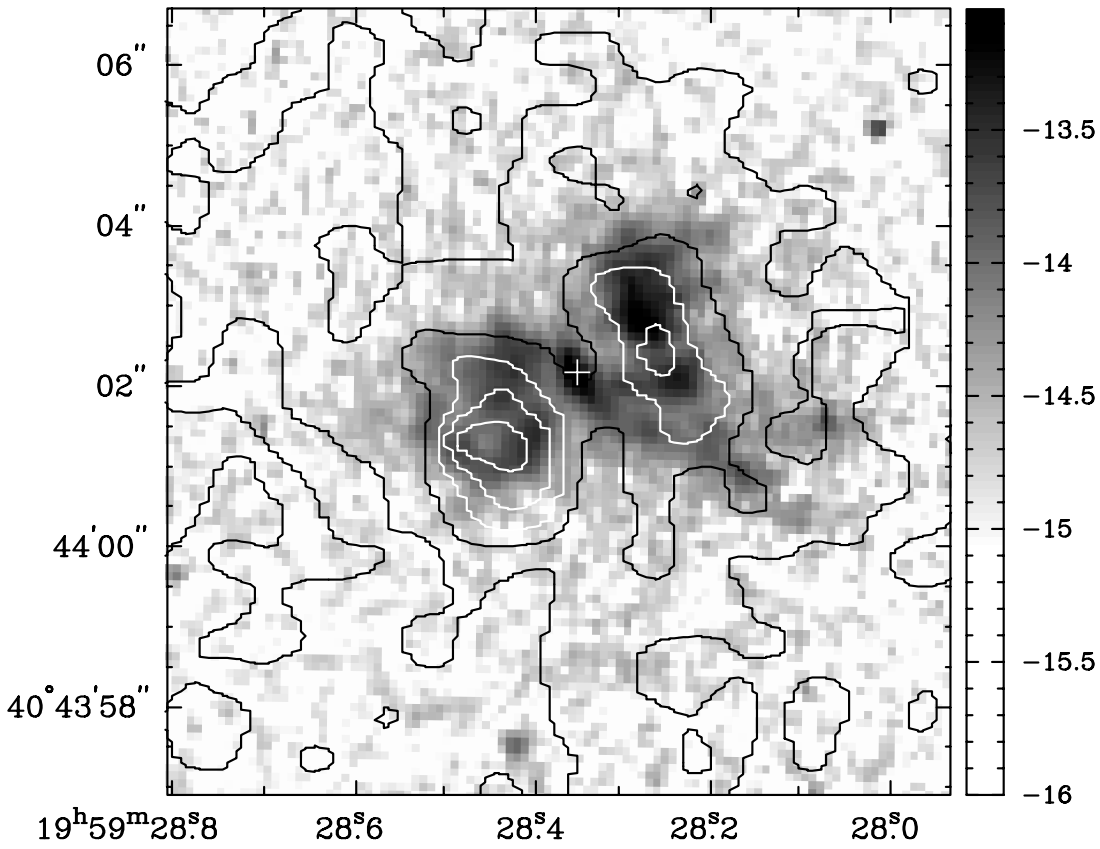

FIG. 10.—Superposition of the *Chandra* 3.2 s frame-time data with events in the range 0.25–1.00 keV (*solid contours*) on an *HST* image taken through a linear ramp filter at redshifted [O III] λ5007 (*gray scale*). The peaks of the 2.00–7.50 keV X-ray emission and the central optical component of the *HST* images were aligned with the radio core (see § 5). The contours are at 2, 6, 10, 14, and 18 counts (0.″5 pixel)$^{-1}$. The *Chandra* image has been resampled to 10 times smaller pixel size and smoothed by a Gaussian of FWHM 0.″5. The optical image has approximately 0.″1 pixel^{-1}. The gray scale of the optical image is proportional to the logarithm of the line intensity and ranges from 1×10^{-16} (*white*) to 9×10^{-14} ergs cm^{-2} s^{-1} arcsec^{-1} (*black*), as indicated by the vertical bar.

than both the Galactic column density to Cygnus A, $N_{\rm H}({\rm Gal}) = 3.3 \times 10^{21}$ cm^2, and the upper limit to the intrinsic column density to the southeast or northwest regions, $\max [N_{\rm H}({\rm SE}), N_{\rm H}({\rm NW})] - N_{\rm H}({\rm Gal}) \lesssim 2.9 \times 10^{21}$ cm^{-2} (see § 4.2). The lack of strong absorption in the *Chandra* soft X-ray spectrum rules out such a high column of *cold*, ionized gas.

As just noted, the observed intrinsic absorbing column density to the soft X-ray emission, assuming the absorbing gas is cold, is $N_{\rm H}({\rm observed, intrinsic}) \lesssim 2.9 \times 10^{21}$ cm^{-2} (see above), while the column density for the scattering medium is inferred to be much larger, $N_{\rm H}({\rm scattering}) \simeq 3.5 \times 10^{22}$ cm^{-2}. This discrepancy may be reconciled if the scattering medium is ionized and hence has a lower opacity to soft X-rays. Ideally, the absorber should be modeled as an ionized gas. However, we can get an idea of the conditions required by writing

$$N_{\rm H}({\rm observed, intrinsic}) = N_{\rm H}({\rm scattering}) \frac{\sigma_{\rm abs}({\rm ionized})}{\sigma_{\rm abs}({\rm cold})} ,$$

where $\sigma_{\rm abs}$(ionized) and $\sigma_{\rm abs}$(cold) are the absorption cross sections of ionized and cold gas, respectively, and bearing in mind that $\sigma_{\rm abs}({\rm ionized})/\sigma_{\rm abs}({\rm cold})$ is a function of energy even for a single ionization parameter for the ionized gas. The absorbing column intrinsic to Cygnus A affects the observed spectrum most in the range $\simeq$0.5–1 keV. At just above $E = 0.5$ keV, $\sigma_{\rm abs}({\rm cold}) \simeq (1\text{–}2) \times 10^{-22}/(E/{\rm keV})^3$ cm^2 (Morrison & McCammon 1983), and $\sigma_{\rm abs}({\rm ionized}) \simeq (2\text{–}3) \times 10^{-23}/(E/{\rm keV})^3$ cm^2 (Krolik & Kallman 1984, their Fig. 4) for a photoionized gas with an ionization parameter (taking into account their different definition of the ionization parameter) of $\xi = L_{\rm X}({\rm nuc})/(n_{\rm H} R^2) \simeq 1$ ergs cm s^{-1}, where $n_{\rm H}$ is the number density of hydrogen nuclei and R is the distance from the nucleus. This ionization parameter corresponds to a plasma temperature of 2×10^4 K, and such a plasma has almost an order of magnitude lower soft X-ray opacity than neutral gas near 0.5 keV. Similarly, at $E = 1$ keV, $\sigma_{\rm abs}({\rm cold}) \simeq 2.4 \times 10^{-22}$ cm^2 and $\sigma_{\rm abs}({\rm ionized}) \simeq 3.6 \times 10^{-23}$ cm^2 for a photoionized gas with $\xi = 63$ ergs cm s^{-1} and $T = 9.1 \times 10^4$ K (again from Krolik & Kallman 1984, their Fig. 4). Thus, such a plasma has almost an order of magnitude lower soft X-ray opacity than neutral gas, but this time at 1 keV. Thus, a conservative lower limit is $\xi > 1$ ergs cm s^{-1}; it is a lower limit because there could be *cold* gas present with the intrinsic column [$N_{\rm H}({\rm observed, intrinsic}) \lesssim 2.9 \times 10^{21}$ cm^{-2}] and *zero* absorption from the scattering column, which would then have to have a very high value of ξ.

The measured unabsorbed X-ray luminosity of the nucleus then implies $n_e R^2 \lesssim 3.7 \times 10^{44} (\xi/1$ ergs cm s$^{-1})^{-1}$ (taking $n_e \simeq n_{\rm H}$). The column density of the scattering electrons $N_e({\rm scattering}) \simeq 3.5 \times 10^{22}$ cm^{-2} corresponds to a number density of $n_e \simeq 11/R$ (kpc) $= 6$ cm^{-3} for the observed $R = 1.9$ kpc. Combining the equations for $n_e R^2$ and $n_e R$, we find $R < 3.4 (\xi/1$ ergs cm s$^{-1})^{-1}$ kpc,

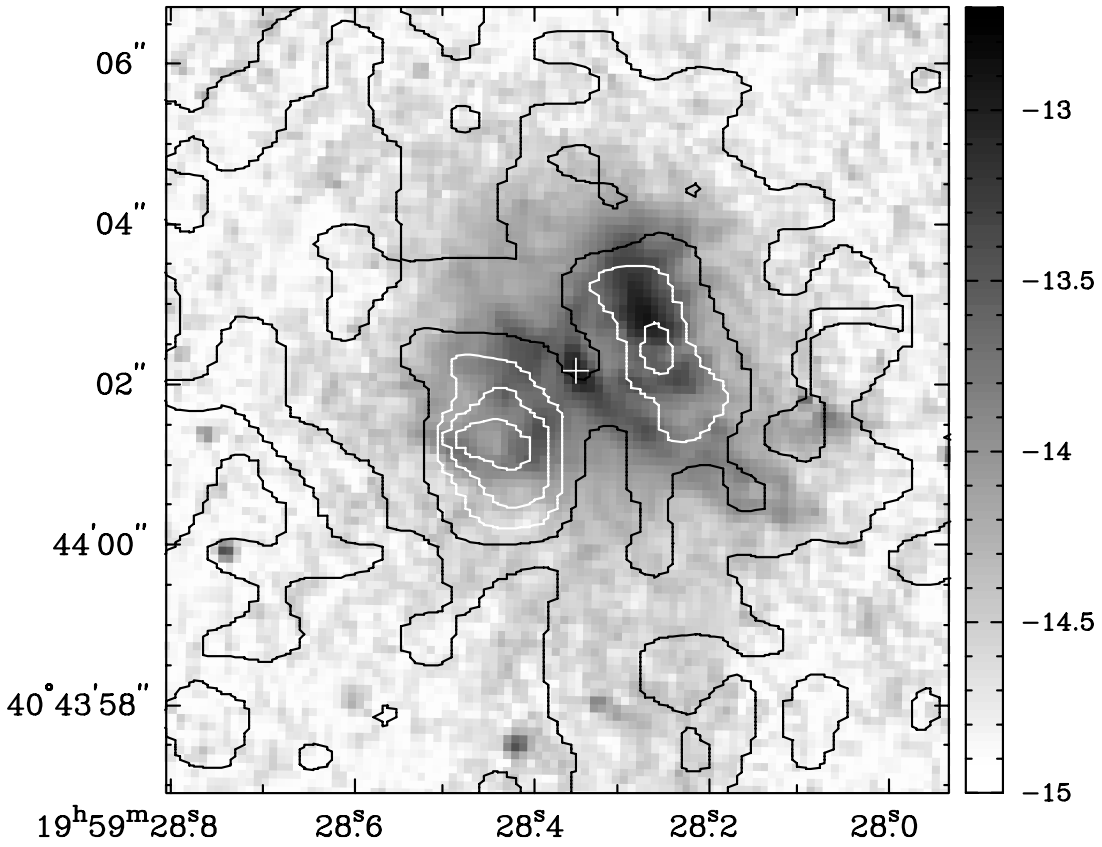

FIG. 11.—Superposition of the *Chandra* 3.2 s frame-time data with events in the range 0.25–1.00 keV (*solid contours*) on an *HST* image taken through a linear ramp filter at redshifted Hα and [N II] λλ6548, 6583 line emission (gray scale). The peaks of the 2.00–7.50 keV X-ray emission and the central optical component of the *HST* images were aligned with the radio core (§ 5). The contours are at 2, 6, 10, 14, and 18 counts (0.″5 pixel)$^{-1}$. The *Chandra* image has been resampled to 10 times smaller pixel size and then smoothed by a Gaussian of FWHM 0.″5. The optical image has approximately 0.″1 pixel^{-1}. The gray scale of the optical image is proportional to the logarithm of the intensity and ranges from 1×10^{-15} (*white*) to 2×10^{-13} ergs cm^{-2} s^{-1} arcsec^{-1} (*black*), as indicated by the vertical bar.

which agrees with the observed distance of the soft X-ray emission from the nucleus if $\xi \simeq 1$ ergs cm s^{-1}. A low value of ξ is consistent with the low ionization state of the Fe Kα line observed from the nucleus and circumnuclear region (see Tables 3 and 5).

The presence of highly ionized Ne lines in the soft X-ray spectrum may be used to constrain the location of gas emitting those lines. To photoionize Ne to Ne VII and Ne X requires 20 ergs cm s$^{-1} \lesssim \xi \lesssim 300$ ergs cm s^{-1} (Kallman & McCray 1982), implying $n_e R^2 \lesssim 1.9 \times 10^{43}(\xi/20$ ergs cm s$^{-1})^{-1}$. If $n_e = 6$ cm^{-3}, we get $R \leq 569$ pc, substantially smaller than the observed nuclear distance of the soft X-ray peaks (Figs. 8–11), which are dominated by continuum radiation. It is possible, however, that n_e may be lower, allowing a larger value of R. This would be the case in a multiphase gas, e.g., with warm dense blobs embedded in a hotter, less dense gas, which would be responsible for the observed highly ionized line emission.

The nuclear absolute magnitude is estimated by Ogle et al. (1997) using the optical polarized flux as

$$M = M_{\rm PF} - 2.5 \log \left(\frac{1}{q\tau P} \right) - A \, ,$$

where $M_{\rm PF}$ is the absolute magnitude of the polarized flux, q is the source covering fraction, τ is the scattering optical depth, P is the intrinsic polarization of the scattered light, and A is the extinction. The observed $M_{\rm PF} = -15.2$ (rest B-band corrected for Galactic extinction, western component only, $H_0 = 50$ km s^{-1} Mpc^{-1}), $P = 11\%$, and $q = 0.86\%$ (Ogle et al. 1997) gives $M_B = -22.8 - 2.5 \log \tau - A_B$. Our estimation of M_B from the SED and this relation suggest that τ is of order 1 if the extinction is small. This τ is much larger than that estimated from the extended soft X-ray emission if the scattering particles are electrons, suggesting instead that the polarized optical light is scattered by dust, unless the value of Ω for the X-rays is much smaller than we assumed.

6.3. *A Nonscattering Origin for the Extended Soft X-Ray Flux*

The extended, soft X-ray emission may also be described by a thermal bremsstrahlung model (see Table 4). The direct bremsstrahlung emission from a plasma with the density inferred in the scattering model ($n_e \sim 6$ cm^{-3}; § 6.2) would dominate over the scattered flux unless the emitting and scattering medium has a temperature below 10^6 K, which is significantly lower than that required in the bremsstrahlung model—$kT = 1.5^{+1.5}_{-0.5}$ keV $\simeq 2 \times 10^7$ K. An argument against the extended emission being entirely due to a thermal plasma is the extremely low metallicity required to provide a good description of the data. A bremsstrahlung model has no metal lines, and the best-fitting MEKAL

model has $Z = 0.03\ Z_{\odot}$. This is unrealistic in what is apparently a metal-rich environment (see Paper III).

6.4. *Conclusions*

We have obtained the highest resolution ($<1''$) image to date of the X-ray emission of the nuclear region of Cygnus A with *Chandra* and also made quasi-simultaneous *RXTE* observations. To summarize, we find the following:

1. The hard X-ray nucleus is located within $0''.4$ of the radio core (i.e., coincident to within the current *Chandra* systematics) and unresolved. The nucleus is well described by a power law of photon index $\Gamma_h \simeq 1.5$ heavily absorbed by a column density of $N_{\rm H} \simeq 2 \times 10^{23}$ cm^{-2}. The rest-frame 2–10 keV unabsorbed luminosity of the nucleus is $L_{\rm X}$(nuc) $\simeq 3.7 \times 10^{44}$ ergs s^{-1}. Emission lines from H-like and/or He-like Ne, highly ionized Si, and "neutral" Fe are observed from the nucleus. A strong Fe K absorption edge is seen, confirming the heavy obscuration of the nucleus.

2. The *RXTE* observations show that the spectrum of the cluster gas may be described by a bremsstrahlung model with temperature $kT \simeq 6.9$ keV and a rest-frame 2–10 keV unabsorbed luminosity of $L_{\rm X}$(cluster) $= 1.2 \times 10^{45}$ ergs s^{-1}. Emission lines from ionized Fe Kα and either or both Ni Kα and Fe Kβ are also observed from the cluster.

3. Bipolar soft X-ray emission is observed to extend $\simeq 1''.2$ toward the northwest and southeast of the nucleus of Cygnus A and aligns well with the bipolar structures seen in optical continuum and line radiation. The bipolar morphology may be produced or enhanced by the passage of a dust lane across the nucleus, providing an additional absorbing column density of $N_{\rm H}$(cold gas in dust lane) $\simeq 2.4 \times 10^{21}$ cm^{-2} and suppressing the very soft X-ray flux. Emission lines from Ne VII–Ne IX, Si II–Si XI, and tentatively H-like Ne are observed in the soft X-ray spectrum of the northwest and southeast regions.

4. Extrapolation of the best power-law model of the soft (0.5–2 keV), extended, circumnuclear emission to higher energies gives a 2–10 keV luminosity of $\simeq 3.7 \times 10^{42}$ ergs s^{-1}, which is 1% of that of the unabsorbed nuclear luminosity in the same band. Furthermore, the photon index (Γ_l) of this soft emission agrees with that (Γ_h) of the directly viewed hard X-ray emission, and so the soft emission is consistent with being electron-scattered X-rays from the nucleus. The scattering region must be ionized to ionization parameter $\xi \gtrsim 1$ in order to be sufficiently transparent to soft X-rays. The column density of the scattering electrons is inferred to be much lower than that required to generate the polarized optical light by electron scattering, suggesting the optical light is, in fact, scattered by dust.

5. The extended soft X-ray emission is well correlated with ionized gas observed optically with *HST*, in particular images in [O III] λ5007 and Hα + [N II] $\lambda\lambda$6548, 6583. This result is consistent with the soft X-ray emitting gas being photoionized.

Future high spectral resolution observations with the *Chandra* and *XMM-Newton* gratings would be able to resolve triplet lines, such as Ne IX, that are good diagnostics of the plasma temperature and the relative importance of photoionization and collisional ionization. In addition, the presence of narrow radiative recombination continua would confirm that the soft X-ray emitting gas is photoionized (see Paerels et al. 2000).

We are grateful to Patrick Shopbell for assistance with the *HST* images and thank A. Stockton for providing electronic versions of his *r*- and *K*′-band images. The VLA radio map was provided in electronic form by R. A. Perley. We thank the referee, Dan Harris, for constructive criticism that improved the clarity and presentation of this paper. Y. T. is supported by a Japan Society for the Promotion of Science Postdoctoral Fellowship for Young Scientists. This research was supported by NASA through grants NAG8-1027 and NAG8-1755.

REFERENCES

Antonucci, R., Hurt, T., & Kinney, A. 1994, Nature, 371, 313
Arnaud, K. A. 1996, in Cygnus A: Study of a Radio Galaxy, ed. C. L. Carilli & D. E. Harris (Cambridge: Cambridge Univ. Press), 51
Arnaud, K. A., Fabian, A. C., Eales, S. A., Jones, C., & Forman, W. 1984, MNRAS, 211, 981
Arnaud, K. A., Johnstone, R. M., Fabian, A. C., Crawford, C. S., Nulsen, P. E. J., Shafer, R. A., & Mushotzky, R. F. 1987, MNRAS, 227, 241
Awaki, H., Koyama, K., Inoue, H., & Halpren, J. P. 1991, PASJ, 43, 195
Awaki, H., Ueno, S., Taniguchi, Y., & Weaver, K. A. 2000, ApJ, 542, 175
Baade, W., & Minkowski, R. 1954, ApJ, 119, 206
Carilli, C. L., Bartel, N., & Linfield, R. P. 1991, AJ, 102, 1691
Carilli, C. L., & Barthel, P. D. 1996, A&A Rev., 7, 1
Dickey, J. M., & Lockman, F. J. 1990, ARA&A, 28, 215
Djorgovski, S., Weir, N., Matthews, K., & Graham, J. R. 1991, ApJ, 372, L67
Elvis, M., et al. 1994, ApJS, 95, 1
Garmire, G. P., et al. 2000, ApJS, submitted
Griffin, R. F. 1963, AJ, 68, 421
Halpern, J. P., Eracleous, M., & Forster, K. 1998, ApJ, 501, 103
Hargrave, P. J., & Ryle, M. 1974, MNRAS, 166, 305
Harris, D. E., Perley, R. A., & Carilli, C. L. 1994, in IAU Symp. 159, Multi-Wavelength Continuum Emission of AGN, ed. T. J.-L. Courvoisier & A. Blecha (Dordrecht: Kluwer), 375
Ho, L. C., & Peng, C. Y. 2001, ApJ, 555, 650
Jackson, N., Sparks, W. B., Miley, G. K., & Machetto, F. 1994, A&A, 284, 65
Jackson, N., Tadhunter, C., & Sparks, W. B. 1998, MNRAS, 301, 131
Jackson, N., Tadhunter, C., Sparks, W. B., Miley, G. K., & Macchetto, F. 1996, A&A, 307, L29
Kallman, T. R., & McCray, R. 1982, ApJS, 50, 263
Krolik, J. H., & Kallman, T. R. 1984, ApJ, 286, 366
Markevitch, M., Forman, W. R., Sarazin, C. L., & Vikhlinin, A. 1998, ApJ, 503, 77
Markevitch, M., Sarazin, C. L., & Vikhlinin, A. 1999, ApJ, 521, 526
Morrison, R., & McCammon, D. 1983, ApJ, 270, 119
Mulchaey, J. S., Koratkar, A., Ward, M. J., Wilson, A. S., Whittle, M., Antonucci, R. R. J., Kinney, A. L., & Hurt, T. 1994, ApJ, 436, 586
Ogle, P. M., Cohen, M. H., Miller, J. S., Tran, H. D., Fosbury, R. A. E., & Goodrich, R. W. 1997, ApJ, 482, L37
Osterbrock, D. E. 1983, PASP, 95, 12
Osterbrock, D. E., & Miller, J. S. 1975, ApJ, 197, 535
Paerels, F., et al. 2000, BAAS, 32, 1181
Perley, R. A., Dreher, J. W., & Cowan, J. J. 1984, ApJ, 285, L35
Ptak, A., Yaqoob, T., Serlemitsos, P. J., Kunieda, H., & Terashima, Y. 1996, ApJ, 459, 542
Reynolds, C. S., & Fabian, A. C. 1996, MNRAS, 278, 479
Sambruna, R. M., Eracleous, M., & Mushotzky, R. F. 1999, ApJ, 526, 60
Shaw, M., & Tadhunter, C. 1994, MNRAS, 267, 589
Smith, D. A., & Done, C. 1996, MNRAS, 280, 355
Smith, D. A., Wilson, A. S., Arnaud, K. A., Terashima, Y., & Young, A. J. 2002, ApJ, in press (Paper III)
Spinrad, H., & Stauffer, J. R. 1982, MNRAS, 200, 153
Stockton, A., Ridgway, S. E., & Lilly, S. J. 1994, AJ, 108, 414
Tadhunter, C. N., Metz, S., & Robinson, A. 1994, MNRAS, 268, 989
Turner, T. J., George, I. M., Nandra, K., & Mushotzky, R. F. 1997a, ApJS, 113, 23
———. 1997b, ApJ, 488, 164
Ueno, S., Koyama, K., Nishida, M., Yamauchi, S., & Ward, M. J. 1994, ApJ, 431, L1
Ward, M. J. 1996, in Cygnus A: Study of a Radio Galaxy, ed. C. L. Carilli & D. E. Harris (Cambridge: Cambridge Univ. Press), 43
Ward, M. J., Blanco, P. R., Wilson, A. S., & Nishida, M. 1991, ApJ, 382, 115
Wilson, A. S., Young, A. J., & Shopbell, P. L. 2000, ApJ, 544, L27 (Paper I)
Young, A. J., Wilson, A. S., & Shopbell, P. L. 2001, ApJ, 556, 6